Monthly Notices
of the
ROYAL ASTRONOMICAL SOCIETY

MNRAS **530,** 3924–3933 (2024) https://doi.org/10.1093/mnras/stae1055
Advance Access publication 2024 April 19

Stellar populations and merger rates of brightest cluster galaxies a billion years ago: SDSS MaNGA IFU spectroscopy

Louise O. V. Edwards ,[1]★ Kevin A. S. J. Hamel,[1] Joseph C. Shy,[1,2] Jonathan Hernandez,[1] Priscilla Holguin Luna,[1,3] Denvir J. Higgins,[1] Theo Chawla,[1] Adriana Gavidia[1] and Samuel Cole[1,4]

[1] *Department of Physics, California Polytechnic State University, 1 Grand Avenue, San Luis Obispo, CA 93405, USA*
[2] *Aerospace Engineering Sciences, University of Colorado Boulder, CO 80309, USA*
[3] *Department of Astronomy, New Mexico State University, MSC 4500, PO BOX 30001, Las Cruces, NM 88003, USA*
[4] *Global Innovation Exchange, University of Washington, Seattle, WA 98105, USA*

Accepted 2024 April 12. Received 2024 March 23; in original form 2023 September 1

ABSTRACT

We investigate the spectroscopic properties of 85 brightest cluster galaxies (BCGs) and their companions observed with the SDSS MaNGA integral field unit. Galaxy redshifts are between $0.08 < z < 0.15$, allowing for a field-of-view up to 80 × 80 kpc. For the main galaxies: the average age of the BCG cores is 7.66 ± 1.36 Gyr with no significant gradient out to 2 $R_{\rm e}$; the average metallicity of the BCG cores is $[Z/H] = 0.23 \pm 0.03$ with a negative gradient of $\Delta[{\rm Z/H}]/\Delta({\rm R/R_e}) = -0.14 \pm 0.09$ which flattens beyond 1.2 $R_{\rm e}$. Velocity dispersion gradients are mostly flat, but a few positive slopes are seen in the most massive galaxies. Emission lines are present in 12 of the BCGs, most often confined to the central ~ 2 kpc with emission line ratios well-described by a LINER or AGN excitation source. There are 78 companion galaxies identified and 9 have nebular emission lines that indicate recent star formation. The companions with flux ratios of 4:1 and 20:1 within 30 kpc of their BCG's core are studied. The companion galaxies have a median age of 7.65 ± 1.55 Gyr and are high-metallicity systems, with a median $[Z/H] = 0.17 \pm 0.07$. Close spectroscopic companions with higher merging probabilities have an average merging time of 0.5 ± 0.2 Gyr. The average merger rate is 0.08 ± 0.12 Gyr^{-1} for 4:1 companions and 0.26 ± 0.22 Gyr^{-1} for 20:1 companions, allowing for an increase in mass of 2.3 ± 3.4 per cent Gyr^{-1} and 3.5 ± 3.2 per cent Gyr^{-1}, respectively.

Key words: galaxies: evolution – galaxies: interactions – galaxies: elliptical and lenticular, cD – galaxies: clusters: general.

1 INTRODUCTION

Observations and simulations of Brightest Cluster Galaxies (BCGs) are consistent with the idea that they form in phases (De Lucia & Blaizot 2007; van de Voort 2016; Ragone-Figueroa et al. 2018; Cooke et al. 2019). The extremely old stellar populations of today's BCG cores (Oliva-Altamirano et al. 2015) imply that the majority of star formation occurred at high-redshift (z) and infrared colours suggest growth of BCGs by star formation at $z > 1$ (Webb et al. 2015) perhaps in a dusty phase (Toft et al. 2014). Models demonstrate that between $1 < z < 2$ star formation and merging contribute equally to the galaxy's mass (Zhao et al. 2017), and observations suggest significant size growth (van Dokkum et al. 2008; van der Wel et al. 2024). Within $z \sim 1$ most mass and size growth then requires a phase of efficient dry merging (Burke & Collins 2013; Ascaso et al. 2014; Lauer et al. 2014; Shankar et al. 2015; Lavoie et al. 2016). Kluge & Bender (2023) argue that the amount of excess light seen in BCG outskirts requires major mergers. Further, multiple cores are prevalent in BCGs (Hsu et al. 2022) and local major mergers (McIntosh et al. 2008; Brough et al. 2011; Jimmy et al. 2013; Liu et al. 2015; Groenewald et al. 2017; Banks et al. 2021) are seen. Yet, Santucci et al. (2023) model the orbits in high mass central galaxies in dense environments to find that both major and multiple minor mergers are important. And, analysis of observations and simulations also shows that minor merging continues to grow BCGs locally (Edwards & Patton 2012; López-Sanjuan et al. 2012; Hilz, Naab & Ostriker 2013), suggesting BCG build-up is an ongoing process.

The age of the galaxy is dominated by the aging stellar populations, but stellar populations may not be uniformly old. Observations (Von Der Linden et al. 2007; Loubser et al. 2009; Oliva-Altamirano et al. 2015; Barbosa et al. 2016) show that a variety of stellar populations contribute to the integrated light, behaviour also predicted in models (Murante et al. 2007; Tonini et al. 2012; Contini et al. 2014). Long-slit studies (Brough et al. 2007; Loubser et al. 2008; Loubser & Sánchez-Blázquez 2012) have found BCG cores have high metallicities, α-enhanced populations, and shallow metallicity gradients. This is interpreted as BCGs having a range of merger histories, with gradients having recently flattened from the effect of mergers as predicted by Hopkins et al. (2009).

Thus, the evolutionary phases and merging history proposed above can be supported or refuted by mapping the stellar populations as a function of radius for BCGs, which is the focus of the present study. Additionally, the companion properties are investigated alongside

---

★ E-mail: ledwar04@calpoly.edu

potential merging activity. Specifically, for a representative sample of 85 BCGs at $z \sim 0.1$, the stellar populations within 1.5 times the BCG's effective radius (R_e) are compared to the properties of their spectroscopic companions. Section 2 describes the data and sample selection. Section 3 describes the methods of removing interloping galaxies and gathering summary statistics for the stellar populations in radial bins. Section 4 presents radial trends of age, metallicity ([Z/H]), and velocity dispersion (σ) for the BCGs, as well as integrated values of age and [Z/H] for the spectroscopic companions. It presents the fraction of BCGs with emission lines. It calculates the number of spectroscopic companions per BCG (N_c). The merger time-scale and dynamical friction time-scale are also calculated leading to merging rates for potential minor mergers, with flux ratios down to 20:1 and potential major mergers with ratios down to 4:1. Summary and conclusions are presented in Section 5. $H_0 = 70$ km s^{-1} Mpc^{-1}, $\Omega_m = 0.3$, and $\Omega_\Lambda = 0.7$ is assumed throughout.

2 DATA AND SAMPLE SELECTION

2.1 SDSS MaNGA

The fourth installment of the Sloan Digital Sky Survey (SDSS-IV) includes a set of 10 000 galaxies with observed integral field spectroscopy (IFU) from the MaNGA survey (Bundy et al. 2015) and instrument (Drory et al. 2015). MaNGA fibre sizes are 2″ in diameter (Westfall et al. 2019), which is well matched to the typical seeing of 1.5″ – 2.0″ (Law et al. 2015). The MaNGA observations were carried out using the Sloan Foundation 2.5-m Telescope, located at Apache Point Observatory in New Mexico, from 2014 to 2020. The observations are dithered in order to sufficiently sample the seeing (Law et al. 2015; Yan et al. 2016). The spatial resolution of the data is measured to be 2.5″ (Goddard et al. 2017b; Westfall et al. 2019), the spectral resolution is $R \sim 2000$, and the spectral window covers 3600 – 10300 Å (Law et al. 2016; Yan et al. 2016).

The sample of brightest cluster (and group) galaxies used here includes 85 galaxies in a redshift range of $0.08 < z < 0.15$ collected from the DR15 public release using the Marvin tool (Cherinka et al. 2019). Marvin provides access to the Data Reduction Pipeline (DRP) and Data Analysis Pipeline (DAP; Belfiore et al. 2019; Westfall et al. 2019) and their results. The DRP processes raw observations to produce flux-calibrated, sky-subtracted datacubes for each of the galaxies in the MaNGA survey. The DAP delivers physical properties derived from the DRP spectroscopic measurements. The two primary objects used in this analysis are Cube and Maps data provided by Marvin. The Cube contains the full spectrum for each spaxel in the observation, whereas the Maps object interfaces with the DAP to produce a 2D 'map' of the galaxy properties. The DAP provides the instrumental resolution-corrected stellar σ [km s^{-1}] as well as emission line fluxes (H β, [O III] 4958Å, [O III] 5007 Å, H α, [N II] 6548 Å, and [N II] 6583 Å) used in the present study.

Petrosian magnitudes, including k-corrections, colours, and effective radii used here are obtained from the NASA–Sloan Atlas[1],compiled by Michael Blanton, called within Marvin.

This study also makes use of the stellar population and kinematic properties obtained from the MaNGA FIREFLY Value Added Catalogue (VAC), computed by Goddard et al. (2017b). The VAC includes the light-weighted age, metallicity, and stellar mass from the full spectral fitting code, FIREFLY (Wilkinson et al. 2017). The stellar population models of Maraston (2011) are used, which are based on the MILES stellar library (Sánchez-Blázquez et al. 2006), with a Kroupa initial mass function (Kroupa 2001). Marvin provides 2D maps of properties from this VAC which are created by the MaNGA DAP through Voronoi binning using the algorithm of Cappellari & Copin (2003) to create cells with a minimum signal-to-noise (SNR) < 10 pixel^{-1}.

2.2 Cluster cross-identification

There are 508 MaNGA galaxies with a redshift > 0.08 and an absolute Petrosian r-magnitude of $M_r < -21.0$ mag. These are used to select bright galaxies in the desired redshift range and are the initial list of BCG candidates. These galaxy positions are searched in the SIMBAD data base[2], 89 sources are identified in SIMBAD as brightest in cluster (BiC) or galaxy in cluster (GiC). Colour–magnitude diagrams of all 89 are constructed to verify whether the chosen galaxy is the brightest in the cluster. The SDSS CasJobs.[3] service is used to collect the positions, magnitudes, and photometric redshifts for galaxies falling within 500 kpc of the potential BCG. At this point all 89 sources were visually examined using an 8′ × 8′ image centred on the candidate (PHL, LOVE). One bright blue spiral was identified and excluded leaving 88 candidates whose images and colour–magnitude diagrams corroborated the BCG status.

The MaNGA sample is cross-matched with the Yang et al. (2007) Sample III SDSS DR7 group catalogue[4] (Yang07). It includes 472 416 groups and clusters with stellar masses between $9.4 < \mathrm{Log}(M_*[\mathrm{M}_\odot]) < 12.9$ and redshifts between $0.01 < z < 0.20$. The final set of BCGs in this study cover $11.9 < \mathrm{Log}(M_h[\mathrm{M}_\odot]) < 15.0$, in halo group mass, with a median of $\mathrm{Log}(M_h[\mathrm{M}_\odot]) = 13.8$ (shown in the top left panel of Fig. 1).

Yang07 flag BCGs in their groups. Of the 88 MaNGA BCGs, 73 match to within 1″ of a Yang07 BCG. The remaining 15 are within 5′ of a Yang07 group centre (which is also true of the Yang07 identified BCGs). The Sample III catalogue gives the largest number of clusters, but the assignment of redshifts given to fibre-collision galaxies can result in erroneous identifications of the Yang07 BCG. To see if the MaNGA BCG might be the more plausible identification, an 8′ × 8′ image around the 15 Yang07 group-centres, which includes the Yang07-identified BCG and the MaNGA BCG, is examined by eye (LOVE). In 5 cases, the Yang07-identified BCG was very close to a bright saturated star, and in all but 3 cases, the MaNGA galaxy is chosen as the more likely BCG as it has a brighter apparent magnitude or appears to be in the geometric centre of the bright cluster galaxies. The three MaNGA galaxies which were identified to be unlikely BCGs for the Yang07 groups are removed from the sample, leaving 85. The above analysis was done using the RA, Dec offsets only. However, the redshifts are used to calculate the velocity offset between the 85 BCGs and the Yang07 group velocity, which is always < 400 km s^{-1}. The final sample of BCGs observed with MaNGA collected for this study is a clean sample of bright, red BCGs, as can be seen in the top panels of Fig. 1 which compares the redshift, brightness, colour distribution, and the halo masses of the selected BCGs to that of the full sample of Yang07 brightest group galaxies. The host group masses of the sample explored in this paper are heavily weighted to the high-mass end of the Yang07 groups. However, the sample is not complete, as it is based only on data that

---

[1] http://www.nsatlas.org/

[2] https://simbad.u-strasbg.fr/simbad/sim-fbasic

[3] https://skyserver.sdss.org/casjobs/

[4] https://gax.sjtu.edu.cn/data/Group.html

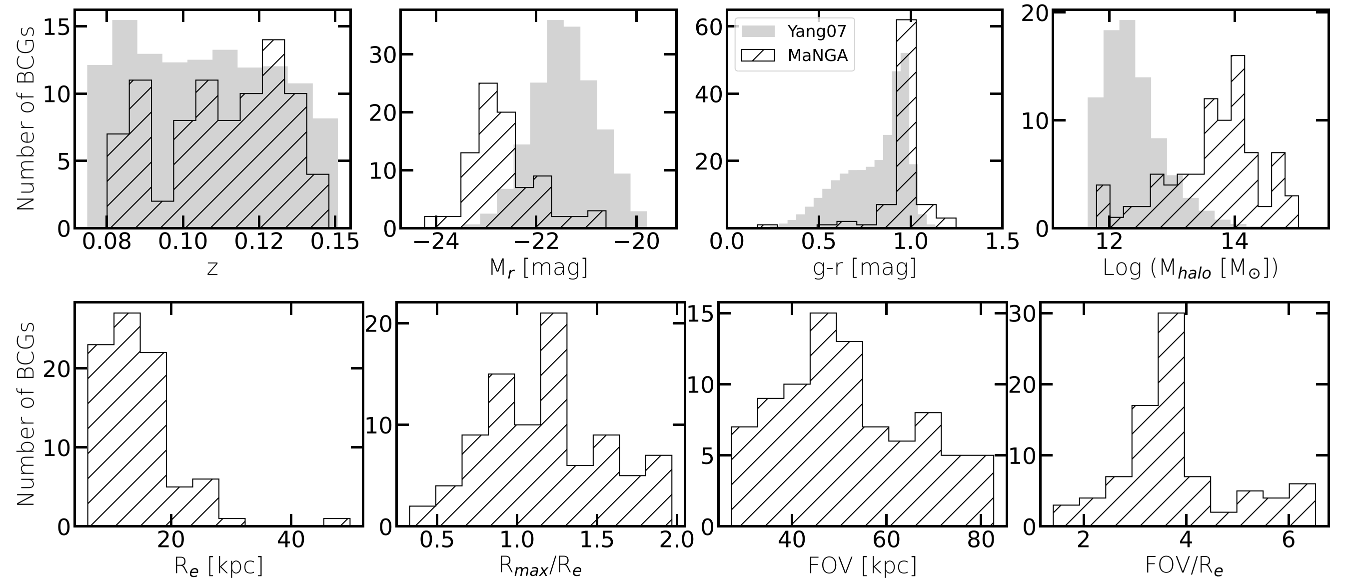

Figure 1. Top: Properties of the MaNGA sample. From left to right, the redshift, galaxy absolute r-magnitude, and g-r colour distributions are shown for the MaNGA BCGs (hashed-black lines) alongside the arbitrarily normalized distribution of the brightest group galaxy from Yang07 sample. The right panel shows the halo masses from Yang07 of the selected MaNGA BCGs (hashed-black lines). The MaNGA selection is indeed dominated by the brightest galaxies and the most massive haloes. Bottom: Galaxy size and FOV. From left to right, for the MaNGA selected sample, the distribution of R_{e}, the ratio of the $R_{\max}/R_{\mathrm{e}}$ (where $R_{\max}$ is the radius out to which the SNR > 3), the distribution of the MaNGA IFU FOV diameter in kpc, and the ratio of the FOV/R_{e} are shown. Most galaxies are observed such that the FOV reaches several times the galaxy's effective radius.

was observed in MaNGA programmes. This may explain why the distribution of absolute magnitude is not smooth in Fig. 1.

The MaNGA galaxy survey limit sets the upper redshift and the lower bound is chosen to maintain a similar physical scale. There are several physical sizes to the MaNGA integral field units (IFUs). In this sample, the IFU diameters range from $12''$ to $32''$, reaching a maximum physical field-of-view (FOV) diameter of up to ~ 80 kpc, as shown in the bottom panels of Fig. 1. The figure also presents the distribution of R_{e}, the ratio of the $R_{\max}/R_{\mathrm{e}}$ (where $R_{\max}$ is the radius out to which the SNR > 3), and the ratio of the FOV/R_{e} for the selected MaNGA BCG sample. Most galaxies are observed such that the FOV reaches several times the galaxy's effective radius.

2.3 Synthetic sky survey Truth and Object catalogues

For comparison, a sample of 123 BCGs in the same redshift and absolute magnitude distributions is collected from the Rubin Observatory's data preview (DP0) available through the Rubin Science Platform[5] The data preview catalogues are derived from a 300 deg^2 synthetic sky survey (Korytov et al. 2019; LSST Dark Energy Science Collaboration (LSST DESC) et al. 2021) based on the OuterRim simulation (Heitmann et al. 2019) which was developed to help test and prepare for the observatory's Legacy Survey of Space and Time (LSST).

The DP0 Object catalogues (LSST Dark Energy Science Collaboration et al. 2021) are created from image simulations, based on the *N*-body simulation, that have been run though realistic observing cadences and then processed with the LSST science pipelines that will be used with the Rubin data releases. The synthetic sky survey contains co-added images at five year depth, with over 110 million extended sources detected and available in the Object catalogues. The DP0.2 Object catalogues, used in this analysis, include photometry and astrometric parameters measured on the co-adds. In this study, the Object catalogues are used to build a sample of BCGs and their projected companions.

The images used for the Object catalogues are derived from simulations, thus DP0 Truth catalogues are also available, which include additional information beyond the photometry, such as 3D positions and noiseless fluxes. In this analysis, the redshift from the DP0 Truth catalogues is used to build a comparison sample of BCG spectroscopic companions from the simulated data.

3 ANALYSIS

This study investigates stellar and kinematic properties of BCG cores, compared to their outskirt regions by building radial profiles of the properties. To limit pollution, bright interloping sources are identified and masked. These potential companions are then further investigated in order to decipher and study spectroscopic companions.

3.1 Identifying the projected companions

An automated process to identify, extract, and mask the IFU fibres containing flux from nearby neighbours is developed in-house. The process identifies local maxima in the SNR map above a given threshold as possible companions. The top panel of Fig. 2 shows a case with 8 local maxima. The central maximum labelled '0' is the BCG. Maxima '1' – '5' have signal that is < 3 times the local value and are not saved as potential companions. The eye spots two companions in the SNR map, these are maxima '6' and '7', for which all spaxels within $3''$ are identified as part of a potential companion. The algorithm then masks these pixels in the Maps to be analysed, such as the σ map in the bottom panel of Fig. 2.

---

[5] https://data.lsst.cloud

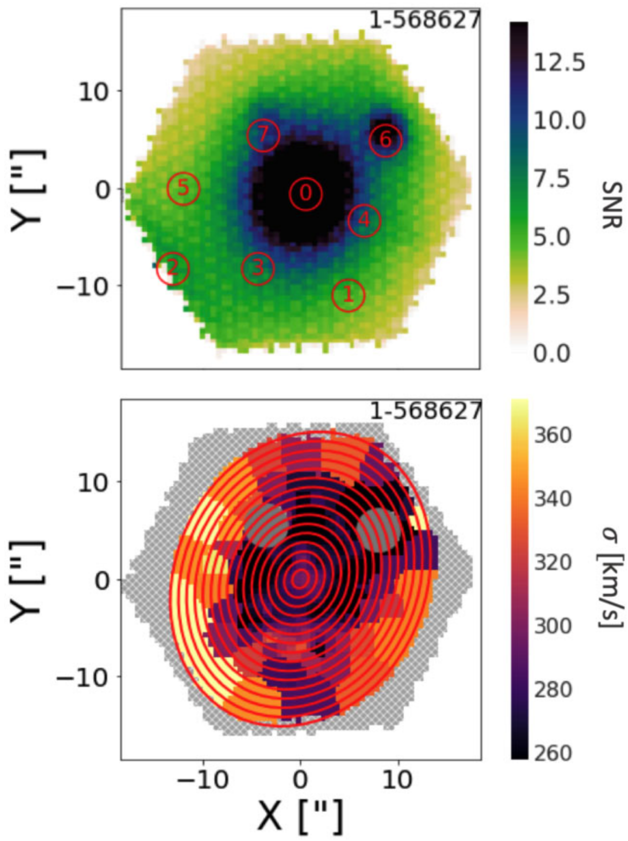

Figure 2. Identifying projected companions. On the top, an SNR map with circular apertures centred on local maxima. Note, the noise level includes the extended light from the BCG and potential companions are identified if their signal rises above 3 times the local value. Thus, objects such as 1 have SNR = 5, but are not included. The circles are illustrative. On the bottom, maxima 6 and 7 have SNR = 12.5 and SNR = 11 and have more than 3 times the flux of their local values, so are counted as potential companions and masked in the analysis of the BCG σ (km s^{-1}).

Each potential companion is confirmed by visual inspection (JH, JCS, KASJH, LOVE) of the MaNGA images. In seven of the 85 systems, there are missing or masked data within core regions of the BCG, with regards to the Maps data. However, the Cube data exists, so the identification of number of companions can still be made. The total number of projected companions identified is 109; 28 BCGs have no companions, 29 have 1 companion, and 28 have 2 or more companions which are masked for the BCG analysis.

3.2 Identifying the spectroscopic companions

Marvin on the Web[6] allows for convenient confirmation of whether the identified companions are true companions or projections. Each of the spectra for the 109 projected companions identified are inspected to ensure that the spectroscopic redshift closely matches that of the BCG, and that the model fits are reasonable. In 26 of the cases, the model fits did not match clear absorption features in the companion spectra, often because of very low SNR or because the galaxies are high-z background galaxies. Four stars and one lower-redshift interloping galaxy were removed. This leaves 78 spectroscopic companions in the sample. It has previously been shown that this simple method of selecting merging pairs based on projected distance and redshift is as good as more complex methods (Pfister et al. 2020).

As a further indication of whether the companions may eventually merge, the probability of the companions being bound is also calculated, using the methods found in Beers, Geller & Huchra (1982) and Brough et al. (2006). Taking the kinetic energy as less than or equal to the gravitational potential energy as a binding criterion, the method considers the solid angle over which this is satisfied, based on the mass and observed velocity difference. Dynamical masses are calculated using equation of Cappellari et al. (2006) and velocity differences are calculated using the radial velocities.

3.3 Building summary statistics

Maps for each property of each galaxy are difficult to display succinctly. Therefore, summary statistics are compiled for the galaxies. For the companions, averages (or sums, where appropriate) from all the spaxels within an aperture are computed. BCG properties are computed in concentric elliptical bins.

3.3.1 Elliptical binning and radial profiles

After masking surrounding companions, radial profiles of stellar properties within the BCG are computed by this team. The signal is stacked within apertures from the galaxy core to the point where SNR < 3. Elliptical apertures with ellipticities specific to the source, gathered from the DAP, are drawn at steps of 0.1 R_e, as illustrated in the bottom panel of Fig. 2. Thus, the central values are an average of the spaxel values within an ellipse that has a major axis of 0.2 R_e. The average R_e for the BCGs in our sample is 7.6″, so that the central bin is ∼1.5″ across, matched to the typical seeing and much larger than the cube's spaxel size of 0.5″. None of the BCGs have R_e that are less than the seeing ($2.8'' < R_\mathrm{e} < 22.7''$). For each ring, the median and standard deviation are calculated, producing the profiles discussed in Section 4.

4 RESULTS AND DISCUSSION

The central age of the BCGs is 7.66 ± 1.36 Gyr and it remains flat and high out to 2 R_e. The central metallicity is $[Z/H] = 0.23 \pm 0.03$, and a negative gradient (-0.14 ± 0.09) is detected which continues to 1.2 R_e, before flattening. Most velocity dispersion profiles are flat, but a few positive slopes are seen in the most massive galaxies. For the companions, the central age and [Z/H] are 7.65 ± 1.55 Gyr and 0.17 ± 0.07, respectively. Seventy eight spectroscopic companions are found within 50 kpc of the 85 BCGs, and have T_merge and $T_{fric} <$ 1 Gyr.

4.1 Radial trends of BCG properties

4.1.1 Absence of age gradients

The top and middle panels of Fig. 3 reveal the old stellar populations and high-central metallicities ubiquitous within the BCGs. This indicates that most of the stars formed very early-on in the universe, in line with recent observations that show massive, well formed BCGs with evolved stellar populations already at $1 < z < 2$ (Joo & Jee 2023). Coogan et al. (2023) have discovered a $z = 1.85$ BGG in the process of assembling, with several components having evolved stellar populations. These observations are consistent with popular formation scenarios where today's dominant galaxies have mainly

---

[6] https://dr17.sdss.org/marvin/

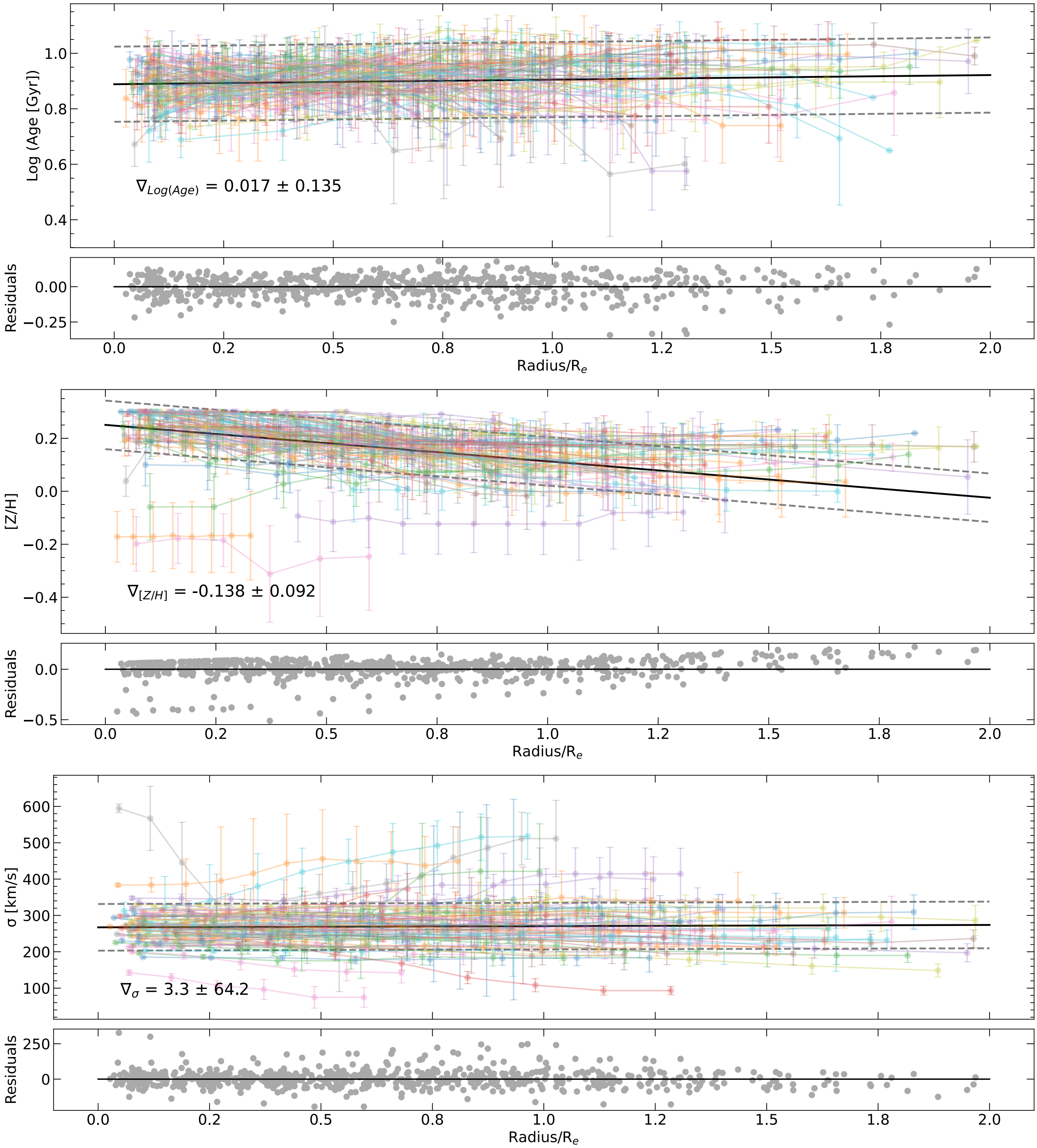

Figure 3. Stellar populations throughout the set of 85 BCGs. Each galaxy is displayed with its own colour, where points and error bars are the average and standard deviation, respectively, of the property values within concentric elliptical bins (see subsection 3.3). From top to bottom, radial profiles of age, metallicity, and velocity dispersion are shown. A best-fitting black line for the sample is overlaid with the standard deviation as dashed-grey lines. The slope and 1σ error for each gradient is shown in on the graphs. The residuals are shown below each profile. A linear, negative metallicity gradient is a good fit within 1.2 R_{e}.

assembled most of their mass early (e.g. Lauer et al. 2014; Toft et al. 2014; Chu, Durret & Márquez 2021), through dry major mergers (e.g. De Lucia & Blaizot 2007; Kluge & Bender 2023).

There is general agreement in the literature, which includes several IFU studies, that shows early type galaxies have flat or very shallow age gradients within 1 R_{e} (see Santucci et al. 2020, and references therein). A nice compilation of results can be found in table 5 of Goddard et al. (2017b) and table 1 of Zheng et al. (2017). The Goddard study also uses MaNGA data with the same VAC results used here, though their sample includes lower redshift galaxies.

Table 1. Property gradients as a function of mass. $\nabla[Z/H] \equiv \Delta[Z/H]/\Delta(\mathrm{R}/\mathrm{R_e})$.

Property	ΔM = Stellar mass	ΔM = Group mass
$\Delta\nabla[Log(Age)]/\Delta M$	0.074 ± 0.1	0.015 ± 0.1
$\Delta\nabla[Z/H]/\Delta M$	-0.072 ± 0.1	0.002 ± 0.1
$\Delta\nabla[\sigma]/\Delta M$	0.184 ± 29.5	29.0 ± 29.2

Within their high mass, early type bin they find $\Delta[\mathrm{age}]/\Delta(\mathrm{R}/\mathrm{R_e}) = -0.066 \pm 0.01$ which agrees with the value from this work of 0.017 ± 0.135. In agreement with recent work by Santucci et al. (2020), data in Table 1 shows no correlation between age gradient and group mass for this sample, though the dispersion in values does increase at higher group mass.

4.1.2 *Shallow, negative metallicity gradients*

Fig. 3 also shows that a shallow, negative metallicity gradient sweeps through the core of the galaxies $< 1\ R_e$. However, a clear break from linearity occurs just past the effective radius, such that by $R/R_e = 1.2$, the profile is flat, with an average value of 0.107 ± 0.113 and the residuals of the linear fit are consistently high. Negative gradients have previously been found in BCGs (e.g. Oliva-Altamirano et al. 2015; Salvador-Rusiñol et al. 2021) and predicted in simulations to flatten from merging activity (Hopkins et al. 2009; Hirschmann et al. 2015). However, previous studies rarely include spectral data beyond $1\ R_\mathrm{e}$ for local BCGs. The BCGs in this study are among the most massive observed with MaNGA and belong to the high mass sample of Oyarzún et al. (2019), who studied 1010 early type MaNGA galaxies. These authors construct a toy model that uses the deviation from linearity to estimate that up to 80 per cent of the starlight in the most massive galaxy outskirts was formed ex-situ (i.e. by mergers). The flattened gradients are not unique to the most massive galaxy of the cluster. Other massive red galaxies in the cluster show gradients, so in that way the BCG may not be special.

Recent studies (Zhao et al. 2017; Goddard et al. 2017a; Li et al. 2018; Santucci et al. 2020) have examined metallicity gradients as a function of environment. All find relatively shallow gradients for early type galaxies with no strong trend with stellar mass when comparing to the same mass range as in the present study. However, Santucci et al. (2020) note that for galaxies in low-mass environments there is a potential weak positive trend such that the gradients become more shallow for higher stellar mass galaxies. Goddard et al. (2017a), alternatively, find no correlation with environment. Here, the metallicity gradients as a function of stellar and group mass are examined, with results shown in Table 1. Though no trend is found with group mass, a weak trend in stellar mass can be seen as only the high-mass galaxies succumb to the steepest gradients ($\Delta[\mathrm{Z/H}]/\Delta(\mathrm{R}/\mathrm{R_e}/M_*) = -0.07 \pm 0.10$). This is also shown in Fig. 4 and suggests that intrinsic conditions dominate over properties of the local environment (group mass), at least within the galaxy's effective radius and within the realm of moderate density environment of high-mass groups.

4.1.3 *Positive velocity dispersion gradients only in most massive galaxies*

The bottom panel of Fig. 3 shows that flat velocity dispersion profiles out to $1\ R_\mathrm{e}$ are common. Tian et al. (2021) studied 54 BCGs in MaNGA noting the same result. That said, there are 6 cases in the present study with positive slopes larger than the standard deviation (1–45787, 1–632309, 1–134760, 1–550913, 1–609414, 1–632513) and three cases with smaller slopes (1–295525, 1–45291, 1–48884).

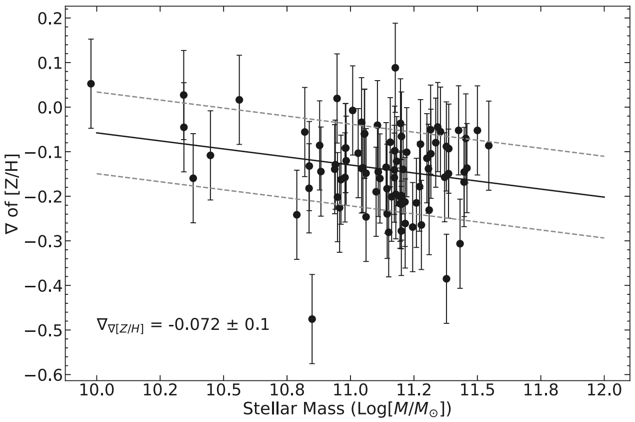

Figure 4. The metallicity gradient as a function of stellar mass. A possible steepening of metallicity gradients with stellar mass can be seen.

Table 2. Stellar mass (Log [M$_\odot$]), average luminosity-weighted age (Log [Gyr]), and metallicity (Z/H) are shown for the 6 galaxies with large positive velocity dispersion gradients. Errors are the standard deviation.

Galaxy	Log(M_* [$M_\odot$])	Log(Age [Gyr])	[Z/H]
1–45787	10.33 ± 0.35	0.88 ± 0.07	0.15 ± 0.02
1–632309	10.01 ± 0.43	0.87 ± 0.06	0.15 ± 0.04
1–134760	10.22 ± 0.39	0.88 ± 0.07	0.12 ± 0.12
1–550913	10.23 ± 0.25	0.86 ± 0.04	0.14 ± 0.06
1–609414	9.56 ± 0.30	0.81 ± 0.03	-0.17 ± 0.02
1–632513	9.10 ± 0.39	0.77 ± 0.09	-0.11 ± 0.02

Table 2 shows that galaxy properties such as stellar mass, age, and metallicity do not unite these systems. For example, a fit of velocity dispersion with stellar mass finds no relationship ($\Delta\sigma/\Delta M_* = 0.18 \pm 64.2$). Further, the range of stellar masses spans $9.10 < \mathrm{Log}(M_*[\mathrm{M_\odot}]) < 10.33$, as can be seen in column 2 of Table 2. The average ages span $-0.765 < \mathrm{Log}\ [\mathrm{Gyr}] < 0.881$ and the average metallicity varies from -0.170 to 0.148.

However, Fig. 5 shows how all six are found in high-mass groups ($\mathrm{Log}(M_*[\mathrm{M_\odot}]) > 11.5$), similar to previous reports (Loubser et al. 2018; Veale et al. 2018; Edwards et al. 2020). In our previous work, the outskirt stellar populations were dominated by intracluster light (ICL). Notably, 1–609414 and 1–632513 have negative age gradients, as commonly seen in the ICL by Montes & Trujillo (2018). As a caveat to this interpretation, the velocity dispersion gradient measurements only extend beyond $1\ R_\mathrm{e}$ for two sources.

4.2 BCG emission lines

BCGs that are co-spatial with large amounts of cooling X-ray gas often show renewed signs of vigor, including strong nebular emission lines (Cowie et al. 1983; Crawford et al. 1999; Hatch et al. 2007; Edwards et al. 2009; McDonald et al. 2010). All BCG spectra were searched for line emission from the Hα-[N II] complex. These lines are identified in 12 of the BCGs, but were usually very weak with only [N II] 6583 Å rising above the continuum level. The emission is confined to the central 2 kpc and the [N II] 6583 Å/Hα ratios are characteristic of excitation by a LINER or AGN source (Kewley,

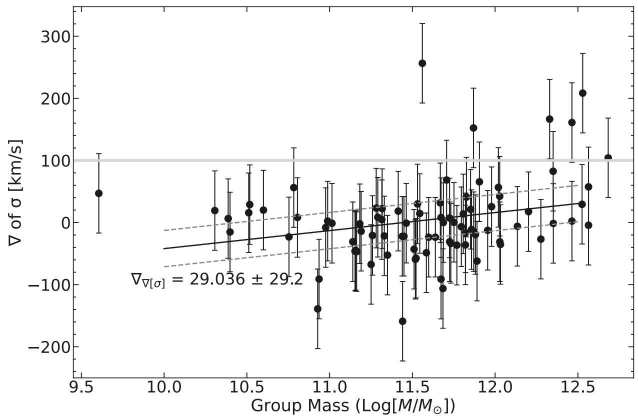

Figure 5. The velocity dispersion gradient as a function of group mass. No evidence for a trend with group mass is seen (see also values in Table 1). However, all the positive gradients (greater than 100 km s^{-1}, above the horizontal grey line) are seen for galaxies in higher mass groups.

Geller & Barton 2006). To check if the emission line galaxies are co-spatial with the peak of the host cluster's X-ray emitting gas, as would be expected in cool-core clusters, the *Chandra* archive[7] was searched. Unfortunately, only nine of the BCGs had data that could be used and no relationship between the presence of emission lines (or colours) and the distance to the X-ray cluster core was found. This could be because the sample is too small.

4.3 Spectroscopic companions

4.3.1 *Properties of spectroscopic companions*

On average, the set of companion galaxies host populations similar to the BCG in age (7.65 ±1.55 Gyr) as seen in Oliva-Altamirano et al. (2015). The average metallicity ($[Z/H] = 0.17 \pm 0.07$) is lower than that of the BCG cores, but Fig. 6 reveals that over half of the companion population hosts high metallicities, similar to the BCG cores. This may be the result of the companion galaxies being high mass elliptical systems. In two cases, the core consists of a double nucleus, with one of the galaxies labelled the companion. Additionally, a companion galaxy in a higher mass cluster could be more massive than a BCG of a lower mass cluster. Nearby companions may be polluted with light from the extensive BCG haloes.

Nine of the spectroscopic companions also have emission lines. In this case, Hα is identified in all but one of the galaxies with the [N II] 6583 Å/Hα consistent with star formation. If companion galaxies do merge with the BCG (as discussed in subsection 4.3.3), they would provide an injection of younger stars into the outer parts of the galaxy, consistent with inside-out formation. That said, the incremental change from such a relatively small population at this epoch is not enough to produce major differences in age for the population, at least within 2 R_e (recall, Fig. 3, top panel).

4.3.2 *Number of companions per BCG (N_c)*

The magnitude differences between the companions and their host BCG are shown in the inset in the bottom of Fig. 6. In considering the completeness of the companions around each BCG, recall from Fig. 1 that the minimum FOV diameter is ∼ 20 kpc. As such, N_c is complete only within a ∼ 10 kpc radius for all 85 BCGs.

For higher values of R_p, complete sub-samples are constructed that include only the galaxies observed with a large enough FOV to catch the potential companions. This reduces the number of BCGs in the N$_c$ calculations at R_p within 30, 25, and 20 kpc to 66, 42, and 24 kpc, respectively. This loss in sample size is reflected in Fig. 7 as increasing error bar sizes, which are calculated from the binomial confidence interval (Cameron 2011).

Fig. 7 shows the main results, N$_c$ for complete sub-samples at various R$_p$. $\mathrm{N}_c = 0.04^{+0.10}_{-0.04}$ for flux ratios down to 4:1, $R_p <$ 30 kpc, relative velocities $\Delta v \leq 300$ km s^{-1}. For 20:1 companions, $\mathrm{N}_c = 0.13^{+0.11}_{-0.07}$. Unless otherwise stated, only companions with high probabilities (> 80 per cent,) are included. N$_c$ for 20:1 flux ratios (including potential minor mergers) and 4:1 ratios (potential major mergers) are shown.

For 4:1 companions, the MaNGA data are consistent with the predictions from the DP0 Truth catalogue (black line). The results also agree with Banks et al. (2021, see also references therein), who measure $N_c = 0.03 \pm 0.01$, for 4:1 GAMA BCG companions within 30 kpc (green star in Fig. 7).

For 20:1 companions, the MaNGA counts are slightly higher than the Truth catalogue (blue line), perhaps indicating pollution from the BCG on faint interloping galaxies. Notice, many MaNGA 20:1 points are most consistent with the DP0 Object catalogue (dashed-blue line). 20:1 companions were investigated by this group (Edwards & Patton 2012, EP12) using the Canada–France–Hawaii Telescope Legacy Survey (CFHTLS). After estimating projection effects, N$_c$ was found to be ∼0.3 for 20:1 companions (R_p < 30 kpc, red squares). The EP12 value is much higher, but note the study focused on a higher redshift bin of $0.15 < z < 0.39$.

4.3.3 *Merger time-scale and merger rate*

The bottom panel of Fig. 6 shows the dynamical friction time-scale (Binney & Tremaine 1987, T_fric) calculated for all companions, with no cut on merging probability and Δv. All but 7 show $T_{fric} < 0.5$ Gyr, which is consistent with EP12 who, using the Millennium simulation (Springel et al. 2005), found that 3D pairs within $r < 30$ kpc have dynamical friction time-scales, $T_{fric} < 0.5$ Gyr. More recently, pair studies have been using the relationship of Kitzbichler & White (2008), who calibrated close pair fractions and merging times (T_merge) also using the Millennium simulation. Calculated using their equations (10) and (11), T_merge ranges from 0.1–1 Gyr, for the MaNGA sample. This provides encouraging evidence between the match of simulation and observation. At $\mathrm{R}_p < 30$ kpc, $\overline{T}_{merge} = 0.50 \pm 0.20$ Gyr such that BCGs experience, on average 0.08 ± 0.12 4:1 mergers per gigayear (0.26 ± 0.22 Gyr^{-1} for 20:1).

The merger rates agree within errors of the value from Liu et al. (2009) of 0.12 ± 0.03 Gyr^{-1}, which includes an overlapping redshift range. Liu et al. (2015) have also reported a value for a higher redshift range, finding 0.55 ± 0.27 Gyr^{-1} at $z \sim 0.43$, where pairs are within $\mathrm{R}_p < 10$ kpc. The merger rate using only MaNGA companions within $\mathrm{R}_p < 10$ kpc is $0.02^{+0.03}_{-0.01}$ and is indeed much smaller than the high-redshift value.

Using the magnitude ratios and merger rates from the $\mathrm{R}_p <$ 30 kpc MaNGA sample, a 5×10^{11} M$_\odot$ BCG would increase its mass by 2.3 ± 3.4 per cent Gyr^{-1} from 4:1 mergers, and by 3.5 ± 3.2 per cent Gyr^{-1}, when including 20:1 mergers. These values are similar to Banks et al. (2021). They are lower than EP12,

---

[7] https://cda.harvard.edu/chaser/

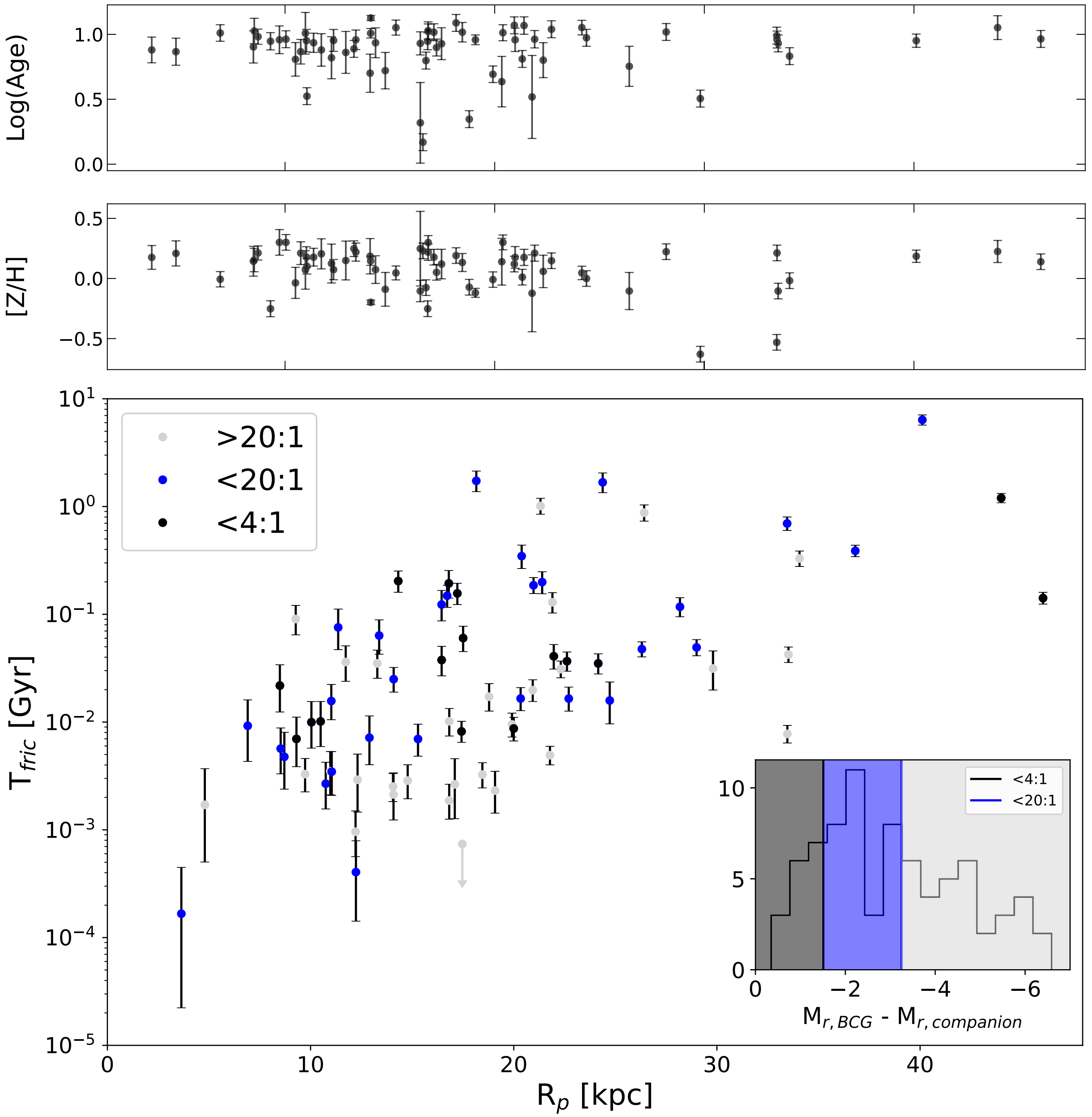

Figure 6. Companion galaxy properties. From top to bottom, the log of age [Gyr], metallicity, and dynamical friction time-scale with distance to the BCG core. Colours represent the flux ratio and the inset defines the colour bins with a histogram of the distribution of r-magnitude differences between the BCG and each companion. The $<$ 4:1 companions are potential major mergers and larger differences are potential minor mergers.

who find 20 per cent Gyr^{-1} at $0.15 < z < 0.39$, and lower than Lidman et al. (2013), who find 35 per cent Gyr^{-1} at $z \sim 1$. The merger rates appear to be dropping since $z \sim 1$.

5 SUMMARY AND CONCLUSIONS

In this paper, stellar populations and merging time-scales of BCGs within $0.08 < z < 0.15$, and their near neighbours, have been determined. The main findings for the BCGs are that the median central age and metallicity are 7.66 ± 1.36 Gyr and 0.23 ± 0.03, respectively, and that by 1.2 R_e, a negative metallicity gradient begins to plateau. The velocity dispersion profiles are overwhelmingly flat, with rising profiles only in six massive groups. Twelve of the BCGs have emission lines revealing central AGN. From 109 projected objects around the BCGs within the MaNGA FOV, 78 are spectroscopic companions. For these, the median age is 7.65 ± 1.55 Gyr and the median [Z/H] is 0.17 ± 0.07. About 8 per cent of the companions show emission lines, and their ratios are consistent with

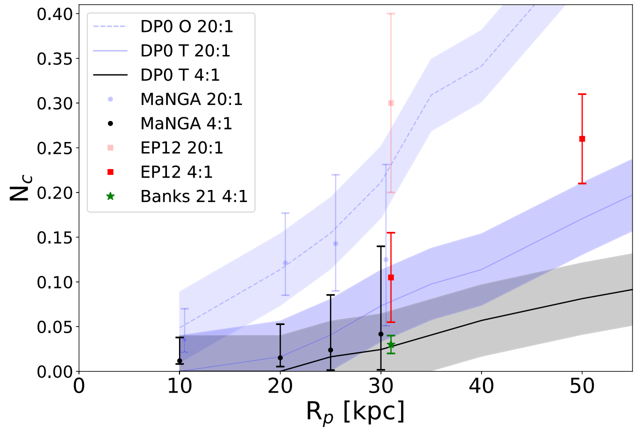

Figure 7. N$_c$ at several values of R_p for major (4:1, black points) and including minor (20:1, blue points) companions. Values from EP12 are shown in red, and from Banks et al. (2021) as a green star. Results from synthetic sky Truth (solid lines) and Object catalogues (dashed line) are shown. Error bars are calculated from the binomial confidence interval.

recent star formation. Within a projected radius of 30 kpc from the BCG, N$_c = 0.04^{+0.10}_{-0.04}$ for 4:1 companions and N$_c = 0.13^{+0.11}_{-0.07}$ for 20:1 companions. Within $\overline{T}_{merge} = 0.50$ Gyr, BCGs experience 0.08 (0.26) 4:1 (20:1) mergers per gigayear, on average, allowing for an increase in mass of 2.3 ± 3.4 per cent (3.5 ± 3.2 per cent).

BCGs and their close companions show old stellar populations, implying their stars formed long ago. A small fraction at $z \sim 0.1$ are still building – at least via dry major and minor mergers – and are expected to consume significant mass over a Gyr. After this period of time, we do not expect the overall stellar populations to change much as the average ages and metallicities of the companions are similar. However, the presence of H α emission lines in companion galaxies, and existence of 4:1 companions suggests examining individual merging systems at this redshift range would be interesting.

ACKNOWLEDGEMENTS

We thank Prof. Sara Brough for the careful and thorough referee report provided that greatly improved this manuscript. This work was partially supported by the SDSS's Faculty And Student Team programme, funded by the Alfred P. Sloan Foundation. We thank Kevin Bundy, Jesus Pando, and Jackie Fraga from that team. LOVE and DJH acknowledge support from an NSF PAARE award #2218943 and RUI #2205976. We thank Melissa Graham for her guidance and leadership at the DP0 assemblies. This research was supported in part by grant number NSF PHY-1748958 to the Kavli Institute for Theoretical Physics (KITP) while LOVE visited as a KITP Fellow. Funding for the SDSS-IV has been provided by the Alfred P. Sloan Foundation, the U.S. Department of Energy Office of Science, and the Participating Institutions. SDSS acknowledges support and resources from the Centre for High-Performance Computing at the University of Utah. The SDSS web site www.sdss.org. SDSS is managed by the Astrophysical Research Consortium for the Participating Institutions of the SDSS-IV Collaboration including the Brazilian Participation Group, the Carnegie Institution for Science, Carnegie Mellon University, Centre for Astrophysics | Harvard & Smithsonian (CfA), the Chilean Participation Group, the French Participation Group, Instituto de Astrofísica de Canarias, The Johns Hopkins University, Kavli Institute for the Physics and Mathematics of the Universe (IPMU)/University of Tokyo, the Korean Participation Group, Lawrence Berkeley National Laboratory, Leibniz Institut für Astrophysik Potsdam (AIP), Max-Planck-Institut für Astronomie (MPIA Heidelberg), für Astrophysik (MPA Garching), für Extraterrestrische Physik (MPE), National Astronomical Observatories of China, New Mexico State University, New York University, University of Notre Dame, Observatório Nacional/MCTI, The Ohio State University, Pennsylvania State University, Shanghai Astronomical Observatory, United Kingdom Participation Group, Universidad Nacional Autónoma de México, the Universities of Arizona, Colourado Boulder, Oxford, Portsmouth, Utah, Virginia, Washington, Wisconsin, as well as Vanderbilt University, and Yale University. This research has made use of data obtained from the Chandra Data Archive and the Chandra Source Catalog, and software provided by the Chandra X-ray Center (CXC) in the application packages CIAO and Sherpa.

6 DATA AVAILABILITY

The data underlying this article were accessed from publicly available catalogues footnoted within the article including the Yang07 group catalogue (gax.sjtu.edu.cn/data/Group.html), the MaNGA data products from Marvin (https://dr17.sdss.org/marvin/), the NASA–Sloan Atlas (http://www.nsatlas.org/), Simbad (https://simbad.u-strasbg.fr/simbad/sim-fbasic), the SDSS SkyServer (https://skyserver.sdss.org/casjobs/), and the *Chandra* X-ray observatory (https://cda.harvard.edu/chaser/). The DP0 data are available to Rubin Data Rights Holders who can apply for an account with the Rubin Science Platform (https://data.lsst.cloud/). The derived data generated in this research will be shared on reasonable request to the corresponding author.

REFERENCES

Ascaso B., Lemaux B. C., Lubin L. M., Gal R. R., Kocevski D. D., Rumbaugh N., Squires G., 2014, MNRAS, 442, 589
Banks K., Brough S., Holwerda B. W., Hopkins A. M., López-Sánchez Á. R., Phillipps S., Pimbblet K. A., Robotham A. S. G., 2021, ApJ, 921, L47
Barbosa C. E., Arnaboldi M., Coccato L., Hilker M., Mendes de Oliveira C., Richtler T., 2016, A&A, 589, 139
Beers T. C., Geller M. J., Huchra J. P., 1982, ApJ, 257, L23
Belfiore F. et al., 2019, AJ, 158, 160
Tremaine Binney , 1987, Galactic Dynamics, Princeton University Press, Princeton, New Jersey USA, , in Spegel D.N., ed., , Princeton University Press, Princeton, New Jersey, USA
Brough S., Forbes D. A., Kilborn V. A., Couch W., 2006, MNRAS, 370, 1223
Brough S., Proctor R., Forbes D. A., Couch W. J., Collins C. A., Burke D. J., Mann R. G., 2007, MNRAS, 378, 1507
Brough S., Tran K.-V., Sharp R. G., von der Linden A., Couch W. J., 2011, MNRAS, 414, 80
Bundy K. et al., 2015, ApJ, 798, L7
Burke C., Collins C. A., 2013, MNRAS, 434, 2856
Cameron E., 2011, PASA, 28, 128
Cappellari M., Bacon R., Bureau M., et al., 2006, MNRAS, 366, 1126
Cappellari M., Copin Y., 2003, MNRAS, 342, 345
Cherinka B. et al., 2019, AJ, 158, 74
Chu A., Durret F., Márquez I., 2021, A&A, 649, 42
Contini E., De Lucia G., Villalobos Á., Borgani S., 2014, MNRAS, 437, 3787
Coogan R. T. et al., 2023, A&A, 677, 3
Cooke K. C., Kartaltepe J. S., Tyler K. D., Darvish B., Casey C. M., Le Fèvre O., Salvato M., Scoville N., 2019, ApJ, 881, L150
Cowie L. L., Hu E. M., Jenkins E. B., York D. G., 1983, ApJ, 272, L29
Crawford C. S., Allen S. W., Ebeling H., Edge A. C., Fabian A. C., 1999, MNRAS, 306, 857
De Lucia G., Blaizot J., 2007, MNRAS, 375, 2

Drory N. et al., 2015, AJ, 149, 77

Edwards L. O. V. et al., 2020, MNRAS, 491, 2617

Edwards L. O. V., Patton D. R., 2012, MNRAS, 425, 287

Edwards L. O. V., Robert C., Mollá M., McGee S. L., 2009, MNRAS, 396, 1953

Goddard D. et al., 2017a, MNRAS, 465, 688

Goddard D. et al., 2017b, MNRAS, 466, 4731

Groenewald D. N., Skelton R. E., Gilbank D. G., Loubser S. I., 2017, MNRAS, 467, 4101

Hatch N. A., Crawford C. S., Fabian A. C., 2007, MNRAS, 380, 1, 33

Heitmann K. et al., 2019, ApJS, 245, 16

Hilz M., Naab T., Ostriker J. P., 2013, MNRAS, 429, 2924

Hirschmann M., Naab T., Ostriker J. P., Forbes D. A., Duc P.-A., Davé R., Oser L., Karabal E., 2015, MNRAS, 449, 528

Hopkins P. F., Cox T. J., Dutta S. N., Hernquist L., Kormendy J., Lauer T. R., 2009, ApJS, 181, 135

Hsu Y.-H. et al., 2022, ApJ, 933, L61

Jimmy, Tran K.-V., Brough S., Gebhardt K., von der Linden A., Couch W. J., Sharp R. G., 2013, ApJ, 778, L171

Joo H., Jee M. J., 2023, Nature, 613, 37

Kewley L. J., Geller M. J., Barton E. J., 2006, AJ, 131, 2004

Kitzbichler M. G., White S. D. M., 2008, MNRAS, 391, 1489

Kluge M., Bender R., 2023, ApJS, 267, 41

Korytov D. et al., 2019, ApJS, 245, 26

Kroupa P., 2001, MNRAS, 322, 231

Lauer T. R., Postman M., Strauss M. A., Graves G. J., Chiasri N. E., 2014, AJ, 797, 82

Lavoie S. et al., 2016, MNRAS, 462, 4141

Law D. R. et al., 2015, AJ, 150, 19

Law D. R. et al., 2016, AJ, 152, 83

Li H. et al., 2018, MNRAS, 476, 1765

Lidman C. et al., 2013, MNRAS, 433, 825

Liu F. S., Lei F. J., Meng X. M., Jiang D. F., 2015, MNRAS, 447, 1491

Liu F. S., Mao S., Deng Z. G., Xia X. Y., Wen Z. L., 2009, MNRAS, 396, 2003

López-Sanjuan C. et al., 2012, A&A, 548, 7

Loubser S. I., Hoekstra H., Babul A., O'Sullivan E., 2018, MNRAS, 477, 335

Loubser S. I., Sánchez-Blázquez P., 2012, MNRAS, 425, 841

Loubser S. I., Sánchez-Blázquez P., Sansom A. E., Soechting I. K., 2009, MNRAS, 398, 133

Loubser S. I., Sansom A. E., Sánchez-Blázquez P., Soechting I. K., Bromage G. E., 2008, MNRAS, 391, 1009

LSST Dark Energy Science Collaboration (LSST DESC) et al., 2021, ApJS, 253, 31

LSST Dark Energy Science Collaboration et al., 2021, preprint (arXiv:2101.04855)

Maraston C., 2011, MNRAS, 418. p.2785

McDonald M., Veilleux S., Rupke D. S. N., Mushotzky R., 2010, ApJ, 721, L1262

McIntosh D. H., Guo Y., Hertzberg J., Katz N., Mo H. J., van den Bosch F. C., Yang X., 2008, MNRAS, 388, 1537

Montes M., Trujillo I., 2018, MNRAS, 474, 917

Murante G., Giovalli M., Gerhard O., Arnaboldi M., Borgani S., Dolag K., 2007, MNRAS, 377, 2

Oliva-Altamirano P., Brough S., Jimmy Tran K.-V., Couch W. J., McDermid R. M., Lidman C., von der Linden A., Sharp R., 2015, MNRAS, 449, 3347

Oyarzún G. A. et al., 2019, ApJ, 880, L111

Pfister H., Dotti M., Laigle C., Dubois Y., Volonteri M., 2020, MNRAS, 493, 922

Ragone-Figueroa C., Granato G. L., Ferraro M. E., Murante G., Biffi V., Borgani S., Planelles S., Rasia E., 2018, MNRAS, 479, 1125

Salvador-Rusiñol N., Beasley M. A., Vazdekis A., Barbera F. L., 2021, MNRAS, 500, 3368

Sánchez-Blázquez P. et al., 2006, MNRAS, 371, 703

Santucci G. et al., 2020, ApJ, 896, L75

Santucci G. et al., 2023, MNRAS, 521, 2671

Shankar F. et al., 2015, ApJ, 802, L73

Springel V. et al., 2005, Nature, 435, 629

Tian Y., Cheng H., McGaugh S. S., Ko C.-M., Hsu Y.-H., 2021, ApJ, 917, L24

Toft S. et al., 2014, ApJ, 782, L68

Tonini C., Bernyk M., Croton D., Maraston C., Thomas D., 2012, ApJ, 759, L43

van de Voort F., 2016, MNRAS, 462, 778

van der Wel A. et al., 2024, ApJ, 960, L53

van Dokkum P. G. et al., 2008, ApJL, 677, L5

Veale M., Ma C.-P., Greene J. E., Thomas J., Blakeslee J. P., Walsh J. L., Ito J., 2018, MNRAS, 473, 5446

Von Der Linden A., Best P. N., Kauffmann G., White S. D. M., 2007, MNRAS, 379, 867

Webb T. M. A. et al., 2015, ApJ, 814, L96

Westfall K. B. et al., 2019, AJ, 158, 231

Wilkinson D. M., Maraston C., Goddard D., Thomas D., Parikh T., 2017, MNRAS, 472, 4297

Yan R. et al., 2016, AJ, 151, 8

Yang X., Mo H. J., van den Bosch F. C., Pasquali A., Li C., Barden M., 2007, ApJ, 671, L153

Zhao D., Conselice C. J., Aragón-Salamanca A., Almaini O., Hartley W. G., Lani C., Mortlock A., Old L., 2017, MNRAS, 464, 1393

Zheng Z. et al., 2017, MNRAS, 465, 4572

This paper has been typeset from a TEX/LATEX file prepared by the author.